Development of a numerical code for laser-induced shock waves applications

S. Bardy, B. Aubert, T. Bergara, Laurent Berthe, P. Combis, D. Hébert, E. Lescoute, Y. Rouchausse, L. Videau

Version of Record: https://www.sciencedirect.com/science/article/pii/S0030399219317712
Manuscript_3166d010cea350e5bb4db22e687140bd

Development of a numerical code for laser-induced shock waves applications

S. Bardy[a], B. Aubert[b], T. Bergara[c], L. Berthe[d], P. Combis[a], D. Hébert[b], E. Lescoute[b], Y. Rouchausse[b] and L. Videau[a]

[a]CEA, DAM, DIF, F-91297 Arpajon, France
[b]CEA, DAM, CESTA, F-33114 Le Barp, France
[c]RESCOLL, 8 Allée Geoffroy, Saint-Hilaire Pessac, France
[d]Laboratoire Procédés et Ingénierie en Mécanique et Matériaux, UMR 8006 CNRS, ENSAM, CNAM, 151 Bd de l'Hôpital, 75013 Paris, France

ABSTRACT

The recent development of LAser Shock Adhesion Test (LASAT) as quantitative Non-Destructive Testing (NDT) process for evaluation of structural bonded assemblies brings new challenges. Applicative assemblies composed of complex materials with poor transverse mechanical properties and highly resistant bonded joints require laser parameters optimization and a more accurate control on the whole process. The development of a numerical tool is then necessary to ensure laser parameters specification to evaluate the bond mechanical strength for a given assembly. In this document, the ability of ESTHER code for the description of laser-matter interaction on aluminum and ablation pressure prediction is exposed. The influence of the target initial reflectivity on ablation pressure is investigated. In this paper, validation of the code in both direct ($1-500\ GW/cm^2$) and water-confined ($0,2-7\ GW/cm^2$) irradiation regimes is achieved with comparison to suitable sets of experimental data. Experiments were led on two laser facilities: the transportable laser shock generator (GCLT) at the CEA/DAM/DIF and the Hephaïstos facility at the Processes and Engineering in Mechanics and Materials laboratory (PIMM lab). Numerical models developed in this work are compared to previous experimental data and to reference models. Ablation pressures defined by our predictive models can then be coupled to other codes which are able to describe 2D/3D shock propagation, in order to model the entire LASAT process on complex assemblies. Characterization of a 6061 Aluminum / Epoxy / 6061 Aluminum assembly is achieved using ESTHER, showing its ability to master the phenomena involved in the LASAT process. For the first time, results open the full numerical design of laser adhesion test with the same code.

1. INTRODUCTION

Transportation sector is currently facing a major challenge: the need to reduce greenhouse gas emissions in a context of significant growth, in particular in civil aeronautics [1, 2, 3]. One way to meet this challenge is to reduce structures' weight [4]. Since the 1970's, civil aircraft structures lightening has been achieved by incorporating composite materials, which exhibit higher specific properties than metallic materials [5]. Composites part has thus increased in such structures from $1-2$ $wt.\%$ to more than 50 $wt.\%$. It is however unlikely that future programs involve even more composites in aircraft structures. Bonding technology appears then as a very promising way to achieve structural lightening. In fact, replacing mechanical fasteners such as bolts and rivets by bonded joints should enable a direct reduction of 12 to 15 % of a civil aircraft structural weight [6]. Nevertheless, bonded joints generalization and their application to critical components implies a need of certification. Nowadays, none of the conventional non-destructive testing (NDT) techniques is able to evaluate mechanical strength. There is therefore a crucial need to develop a NDT technology capable of bonded assemblies quantitative evaluation. The development of the LAser Shock Adhesion Test (LASAT) on bonded assemblies with NDT concerns must answer this challenge [7].

LASAT process is based on both shock generation by laser-matter interaction and shock propagation within multi-materials stacks. Focusing a pulsed laser beam of several J to several tens of J during some ns on a spot of some mm^2 of a metallic target enables heating the matter from solid to plasma state [8]. The rapid ejection of vapor from the

laurent.berthe@ensam.eu (L. Berthe)
ORCID(s):

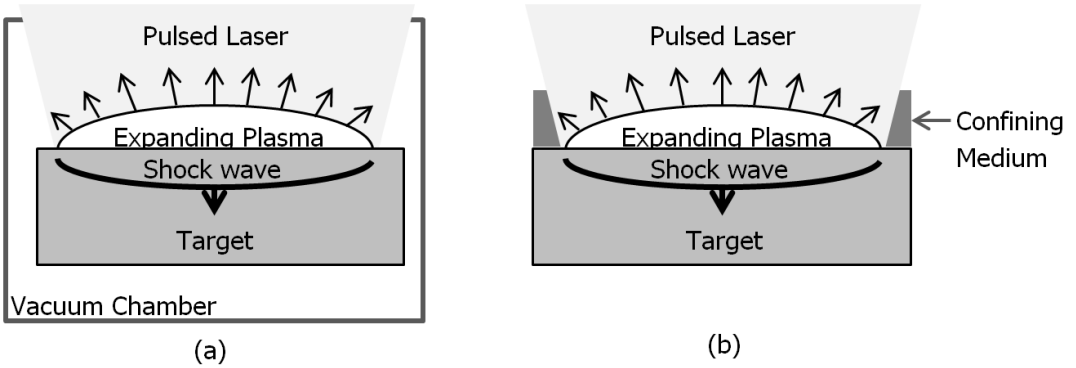

Figure 1: Schematic view of the generation of a shock wave induced by laser (a) in direct interaction regime, (b) in water-confined regime

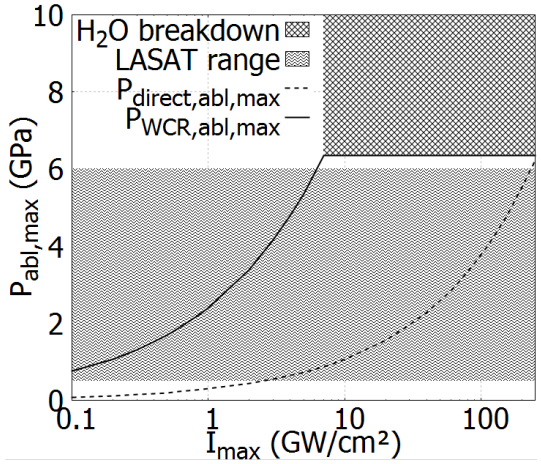

Figure 2: Typical pressure laws $P_{abl,max}$-I_{max} extracted from models developed here, in both direct interaction configuration and WCR - temporal Gaussian pulse - $\tau = 7\ ns$ FWHM - $\lambda = 532\ nm$ - Identification of the LASAT working range and water breakdown range

target front face implies the application of a reaction force on the illuminated surface [9, 10, 11]. The resulting ablation pressure (P_{abl}) exhibits roughly the same properties as the laser pulse: a fast loading ramp ($1-2\ ns$) combined to a high amplitude (maximal ablation pressure ($P_{abl,max}$) of several GPa), typical of a shock wave. Two different interaction regimes are identified for laser-induced shock wave generation: the direct illumination regime, performed in vacuum conditions as presented in Figure 1 (a), and the Water-Confined Regime (WCR) (Figure 1 (b))[12].

In the last case, the confining medium prevents plasma expansion and hence maximizes ablation pressure amplitude and duration [12, 13, 14]. As exposed on Figure 2, WCR requires then lower intensities ($0\ GW/cm^2 < I_{max} < 7\ GW/cm^2$) than the one used in direct interaction regime ($0\ GW/cm^2 < I_{max} < 500\ GW/cm^2$) to cover the typical LASAT ablation pressure range ($0,5-6\ GPa$). WCR is also employed for Laser Shock Peening (LSP) applications in the same range of laser pulse duration and intensities. WCR is thus preferred for industrial applications since it enables the use of compact laser facilities and is easily integrable to production or maintenance environments. Previous studies have highlighted the existence of plasma breakdown threshold at higher intensities ($I_{max} > 7\ GW/cm^2$) which limits shock generation in these conditions [15, 16, 17]. In this study, all investigations were led under this threshold.

The second part of LASAT process lies on the propagation, transmission, reflection and attenuation of the front face-generated shock wave within the considered multi-materials stack. In acoustic propagation hypothesis, matter is subjected to compression stresses after a shock wave passes through it. Stresses diminishes then with release waves which follows the shock wave front. The incident shock wave is reflected in release wave at the free surface, on the

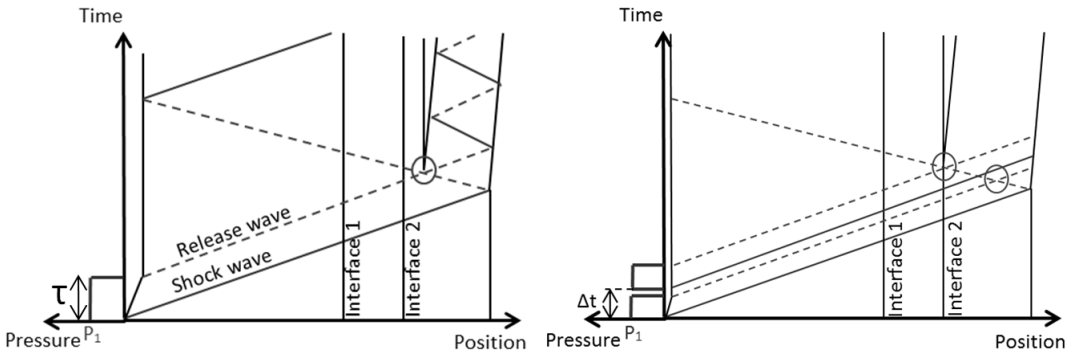

Figure 3: Schematic Time-Position diagrams showing shock and release waves travels in a multi-materials target (a) in a typical ns-pulse configuration with τ the pulse duration, (b) in double frontal pulse configuration, with Δt the delay separating the two ns-pulses

target back face. Recombination of both incident and reflected release waves induces tensile stresses, which can lead to target spallation, and enables thus to test an interface [18]. It is therefore possible to steer tensile stresses amplitude and position with laser parameters.

In the case of bonded assemblies implying thick substrates ($>> 0,1\ mm$) of complex materials such as stratified composite, typical *ns*-laser pulse induces preferentially an intra-substrate failure, as shown on Figure 3 (a). Indeed, in this case, the recombination zone is located in the back face substrate which exhibits intra-laminar mechanical strength very close to bond mechanical strength. Previous studies have demonstrated the interest of laser parameters optimization to localize tensile stresses on the bonded joint [19, 20]. The double frontal pulse configuration has been identified as the ideal configuration, easier to use with access to one face only, as exposed on Figure 3 (b). Taking into account the complexity of composites' behavior under shock loading and the requirement for weak bond discrimination with just-below-tolerance mechanical strength (about 80 % of the correct mechanical strength), optimizing laser parameters in double-pulse configuration and mastering more accurately the whole LASAT process are two essential requirements. In the frame of an industrial exploitation of the process, an automatic numerical tool, integrating predictive models, is the unique solution for laser parameters optimizing, regarding a given application. No existing numerical laser-matter interaction models have proven to be predictive in the here-above mentioned configuration of interest. A previous numerical model, developed for mono-pulse ablation pressure prediction, produced results in good accordance with experimental results [21, 22, 23]. However, it doesn't describe shock waves propagation on *mm*-thick samples and was never evaluated in double-pulse configuration. It is thus inappropriate for the here-above described application.

The development of such numerical models for both direct interaction regime and WCR is shown here. The numerical tool used in this study for model development is ESTHER code. It is a Lagrangian mono-dimensional code able to describe radiation-matter interaction and shocks propagation in targets. It was initially developed at the CEA/DAM/DIF for femtosecond laser-matter interaction modeling [24, 25, 26]. It has also been used to simulate nanosecond laser-matter interaction in a high intensity range [27]. In our intensity range, a previous study was led with this code to highlight the influence of material properties on the ablation pressure determination process based on rear Free Surface Velocity (FSV) measurements [28]. This previous study also enabled to demonstrate ESTHER capacity of ablation pressure prediction on aluminum in the $50 - 500\ GW/cm^2$ range, identified as the typical range used in laser-induced shock wave experiments. This paper presents Esther code validation at even lower intensities to cover the $0 - 500\ GW/cm^2$ range in direct regime and the $0 - 7\ GW/cm^2$ in WCR on aluminum. The influence of physical phenomena on the ablation pressure is exposed and comparison of laser-matter interaction models with previous results is also achieved in both direct and WCR regimes. Finally, they are coupled to appropriate materials models and used for characterization of a 6061 Aluminum / Epoxy / 6061 Aluminum assembly. So, ESTHER has already been widely used to study the matter laser interaction in many conditions. This paper aims to demonstrate for the first time its ability to simulate all phenomena related to adhesion test techniques including material laser interaction, propagation in assemblies and damage to interface opening tools to design adhestion laser shock testing.

2. NUMERICAL TOOL

2.1. Modeled physical phenomena in ESTHER

2.1.1. Laser propagation and energy deposition

Laser propagation through matter is modeled by solving Helmoltz equation on each cell. Equation 1 represents Helmholtz relation which determines the absorbed part of the incident amount of energy entering in each cell. $\overrightarrow{E_0}$ is the laser field, ω_0 the pulsation associated to the laser field, c the light velocity and $\tilde{n}$ the complex index. $\tilde{n}$ is defined by Equation 2 with n_1 the real index and n_2 the imaginary index.

$$\Delta\overrightarrow{E_0} + (\frac{\omega_0}{c}\tilde{n})^2\overrightarrow{E_0} = 0 \tag{1}$$

$$\tilde{n} = n_1 + i.n_2 \tag{2}$$

In ESTHER, n_1 and n_2 can be determined in a large range of matter states. Solid indexes are defined using E.D. Palik tables [29]. Plasma indexes are determined using Equation 3 and Equation 4, where n_e is the electronic density, n_c the critical electronic density and ν_{ei} the electron-ion collision frequency.

$$n_1 = \sqrt{1 - \frac{n_e}{n_c(\omega)}} \tag{3}$$

$$n_2 = \frac{1}{2}\frac{n_e/n_c(\omega)}{\sqrt{1 - n_e/n_c(\omega)}}\frac{\nu_{ei}}{\omega} \tag{4}$$

These two last terms are calculated by the code with Equation 5 and Equation 6, typical of the Lorenz plasma model [30]. In these expressions, m_e is the electron mass, Z the atomic number of the considered material, e the electronic charge, $ln\Lambda_{ei}$ the electron-ion Coulomb logarithm, k_b Boltzmann constant and T the cell temperature.

$$n_c = \frac{\omega^2 m_e \epsilon_0}{e^2} \tag{5}$$

$$\nu_{ei} = \frac{4/3\sqrt{2\pi}n_e Z e^4 ln\Lambda_{ei}}{(4\pi\epsilon_0)^2\sqrt{m_e}(k_b T)^{3/2}} \tag{6}$$

In the Warm Dense Matter (WDM) field between solid and plasma state, indexes are determined by interpolation. Absorption of laser light is therefore calculated in a wide range of conditions. In addition, the method described here permits also to take into account reflection phenomenon at interfaces, defining the reflectivity (R) at normal incidence of each cell using Equation 7 [31].

$$R = \frac{(n_1 - 1)^2 + n_2^2}{(n_1 + 1)^2 + n_2^2)} \tag{7}$$

The ability to describe matter state evolution from solid to plasma state and reflection phenomena enables to model laser propagation on the whole range of states concerned by our application: from laser-metal to laser-plasma interaction. Continuities relationships are applied at cell interfaces and permit then to describe laser propagation through a stack of cells, defining reflection, absorption and transmission of laser light in each cell, as shown on Figure 4.

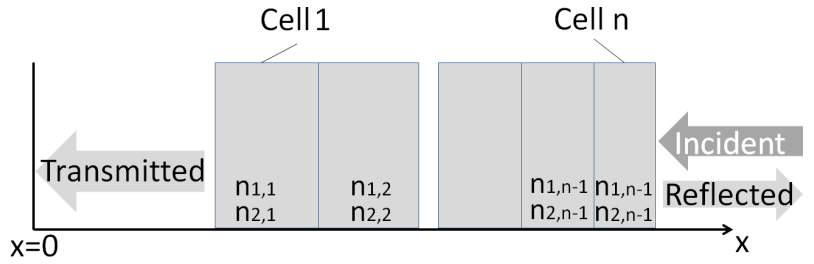

Figure 4: Schematic view of the propagation of an incident laser pulse through a stack of n cells, with optical indexes $n_{1,i}$ and $n_{2,i}$ determined for each cell ($1 \leq i \leq n$)

2.1.2. Hydrodynamics

In ESTHER, hydrodynamics is described by solving the equation of cell position evolution (Equation 8) and conservation equations for mass (Equation 9), momentum (Equation 10) and energy (Equation 11) on finite volumes in planar mono-dimensional hypothesis. In these equations, r is the cell position, t the time, u the material velocity, ρ is the density, P the pressure, Q the pseudo-viscosity, D the deviatoric stresses and e the internal energy.

$$\frac{\partial r}{\partial t} = u \tag{8}$$

$$\frac{\partial \rho}{\partial t} + \frac{\rho}{r}\frac{\partial (ru)}{\partial r} = 0 \tag{9}$$

$$\frac{\partial u}{\partial t} + \frac{1}{\rho}\frac{\partial (P + Q - D)}{\partial r} = 0 \tag{10}$$

$$\frac{\partial e}{\partial t} + \frac{P + Q - D}{\rho r}\frac{\partial (ru)}{\partial r} = 0 \tag{11}$$

These conservation equations are coupled to Equations Of State, solved on finite volumes, permitting to describe hydrodynamics in the cell stacking. Three types of EOS are available in ESTHER: perfect gas EOS, Puff-Mie-Grüneisen (PMG) EOS and tabulated EOS. PMG EOS enable to describe matter state close to ambient conditions ($P_0 = 10^5\ Pa$, $T_0 = 300\ K$). Tabulated EOS establish relationships between density, pressure, temperature and internal energy. Associated data are representative of matter state in conditions far from ambient ones, typical of laser-matter interaction-generated plasmas. These tabulated EOS take also into account solid/liquid and liquid/vapor state transitions. Bushman-Lomonosov-Fortrov EOS (BLF) and Sesame EOS transmitted by the Los Alamos National Laboratory (LANL) are very close to each other in the case of aluminum. Minor divergences exist around state transitions but the effects of such differences are negligible in the considered regime of intensities. These two EOS can thus be employed to model hydrodynamics in matter subjected to significant changes due to laser illumination on the target front face.

2.1.3. Energy transfer

In ESTHER, two types of energy transfer phenomena are implemented: thermal conduction and radiative transfer. Thermal conduction is driven by conductivity, calculated at interfaces as an harmonic mean, following Equation 12, where $K_{ther,i+\frac{1}{2}}$ is the mean conductivity at the considered interface, $K_{ther,i}$ the conductivity of one cell and $K_{ther,i+1}$ of the cell on the other side of the considered interface. Thermal conductivity (K_{ther}) is determined in each cell, taking into account matter state. In solid state, data are extracted from Y.S. Touloukian tables [32]. In plasma state, data are determined from tabulated data, generated by the atomic physics SCAALP code [33], [34]. Thermal conductivity can

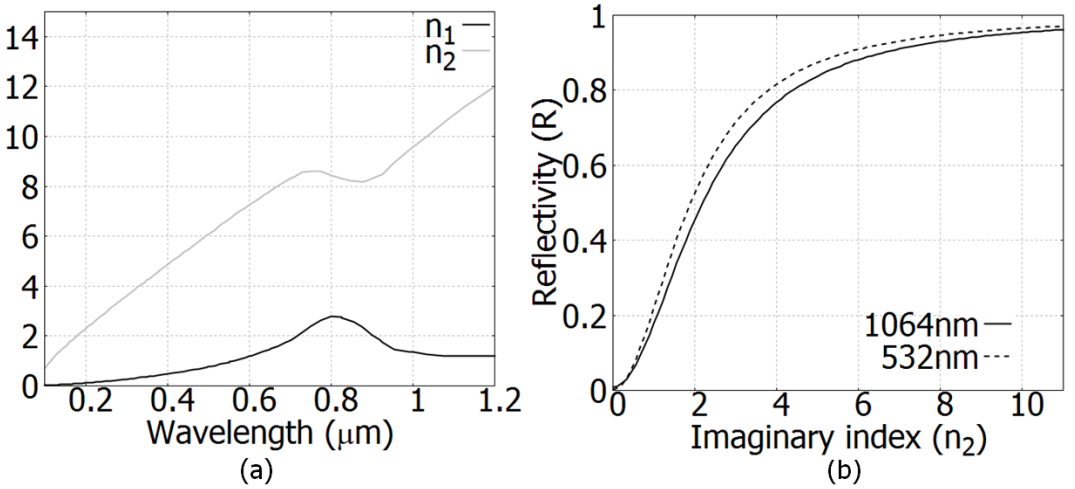

Figure 5: (a) Evolution of optical real (n_1) and imaginary (n_2) indexes with the wavelength (λ) for pure aluminum according to E.D. Palik tables [29] and (b) Evolution of reflectivity (R) with the imaginary index (n_2) for $\lambda = 532\ nm$ and $\lambda = 1064\ nm$ for pure aluminum with n_1 determined by E.D. Palik tables [29]

thus be calculated for a wide range of matter states, enabling the description of thermal conduction in the plasma and beyond, in the ablation zone.

$$K_{ther,i+\frac{1}{2}} = \frac{2K_{ther,i}K_{ther,i+1}}{K_{ther,i} + K_{ther,i+1}} \tag{12}$$

Radiative transfer model in ESTHER is based on the so-called "SN" method [35]. Opacities and emissivities are calculated by using the Nohel code, developed at the CEA/DAM/DIF [36]. Radiative transfer is activated as soon as at least one cell reaches a threshold temperature (typically 2eV).

2.2. Influence of initial reflectivity

2.2.1. Reflectivity-Roughness dependance - Implementation in ESTHER

Initialization of the target front face reflectivity is achieved using E.D. Palik tables. These tables determine optical indexes n_1 and n_2 for a given material and a given wavelength (λ). As precised before, these data consider a light beam with normal incidence on a perfectly flat surface. However, a previous study has highlighted how the surface state, *e.g.* roughness, can affect the apparent reflectivity [37]. This study demonstrates that a rough surface induce multiple reflections/absorptions of a single laser beam, due to local incident angle modification. Absorptivity is then enhanced, traducing a decrease of the apparent reflectivity. In order to take into account the initial surface state of the target in our model, solid reflectivity is directly steered by the modification of n_2. On Figure 5 (a), both n_1 and n_2 evolutions with wavelength are exposed for the case of a pure aluminum target, according to E.D. Palik tables. For the same material, Figure 5 (b) shows the evolution of the reflectivity (R) with n_2 variations, according to Equation 7 and keeping n_1 as defined by E.D. Palik tables, for the two wavelengths usually employed in laser-induced shock experiments ($\lambda = 532\ nm$ and $\lambda = 1064\ nm$). We notice that $R = 0,92$ for $\lambda = 532\ nm$ with $n_2 = 6,4$ (Palik value) and $R = 0,95$ for $\lambda = 1064\ nm$ with $n_2 = 10,0$ (Palik value). Decreasing n_2 enables to steer R easily from the above-mentioned value to 0. Using this method permits to take indirectly into account the initial reflectivity state of the target in ESTHER simulations.

2.2.2. Reflectivity influence on ablation pressure

The influence of initial reflectivity on the ablation pressure process has been investigated by performing simulations in direct irradiation regime with $\lambda = 1064\ nm$ at various maximal intensities (I_{max} = 1,10 and 100 GW/cm^2) for temporal top-hat pulses of duration $\tau = 10\ ns$. Intensity ramp from $I = 0$ to $I = I_{max}$ has a voluntarily-fixed duration at 10 fs, in order to minimize intensity ramp-induced effects. The decrease slope at the end of the pulse is linear with

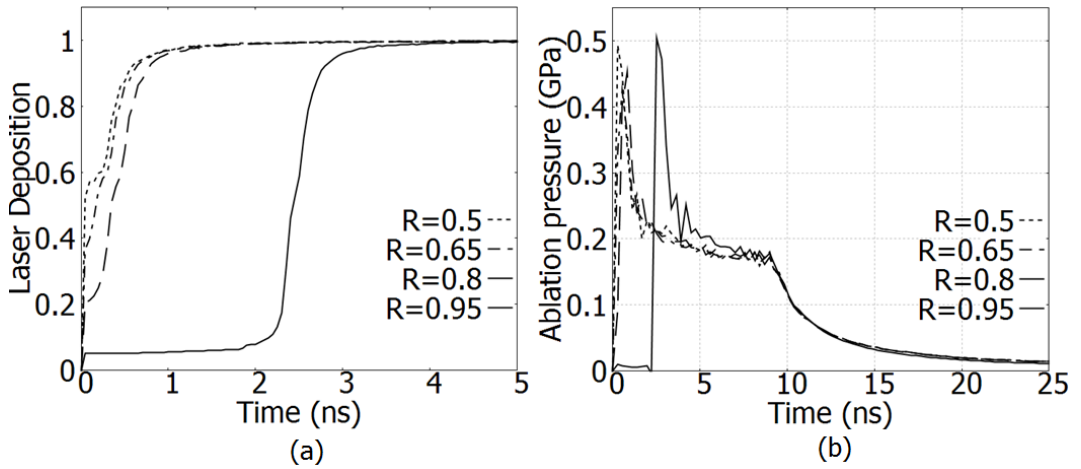

Figure 6: Influence of initial reflectivity on (a) laser deposition and (b) ablation pressure on pure aluminum target - $\lambda = 1064\ nm$ - $I_{max} = 1\ GW/cm^2$ - $\tau = 10\ ns$ - $R = 0,5,\ 0,65,\ 0,80,\ 0,95$

Table 1
Theoretical (Palik-based [29]) and experimental results of aluminum initial reflectivity

	$\lambda = 532\ nm$	$\lambda = 1064\ nm$
Theoretical	0,92	0,96
Experimental	0,4 (+/-0,1 mm)	0,52 (+/-0,1 mm)

a duration of 1 ns, which is typical of experimental temporal top-hat pulses. In each configuration, a variation of R is applied ($R = 0,5,\ 0,65,\ 0,8,\ 0,95$) and resulting ablation pressures are extracted from simulations and compared to each other. At low intensities ($I_{max} = 1\ GW/cm^2$), the initial reflectivity has a significant influence on ablation pressure. We notice on Figure 6 that lowering initial reflectivity implies more laser absorption and hence more energy deposition in aluminum at the beginning of the laser pulse. This phenomenon finally participates to a faster matter heating, state changes and plasma generation, in particular between $R = 0,95$ and $R = 0,8$ since absorption at solid state varies of a factor 4 between those two values. The resulting ablation pressures durations are consequently longer for lower reflectivities since the shock front corresponding to plasma generation appears sooner.

3. RESULTS AND DISCUSSION

3.0.1. Initial reflectivity definition

Reflectivity measurements were achieved at the two wavelengths of interest for the present work ($\lambda = 532\ nm$ and $\lambda = 1064\ nm$) on aluminum targets by two previous studies [17, 38]. A synthesis of these measurements at solid state is exposed in the Table 1. These results confirm the difference existing between theoretical results and experimental results and highlight the need to consider lower-than-theoretical initial reflectivity to correctly reproduce low-intensity laser-matter interaction. $R = 0,5$ was used in ESTHER for $\lambda = 532\ nm$ WCR experiments and $R = 0,6$ was employed to reproduce $\lambda = 1064\ nm$ direct interaction experiments. The corresponding results are presented in the two following subsections.

3.1. Direct interaction regime

3.1.1. Experimental facility

The experimental facility used to perform direct irradiation experiments is the transportable laser shock generator (GCLT) of the CEA (Alternative Energies and Atomic Energy Commission). The Nd:YAG source of this facility delivers $1064 - nm$ laser pulses up to 40 J with on-demand pulse durations from $5-$ to $100 - ns$. The laser-pulse temporal profile can be designed in order to produce Gaussian-like, triangle or top-hat pulses. A vacuum chamber is employed to ensure direct interaction of the laser beam with the target. In this study, phase plates adapted to spot diameters (ϕ) from 1 mm to $3,2\ mm$ and CCD cameras were used to master and control the on-target spatial energy

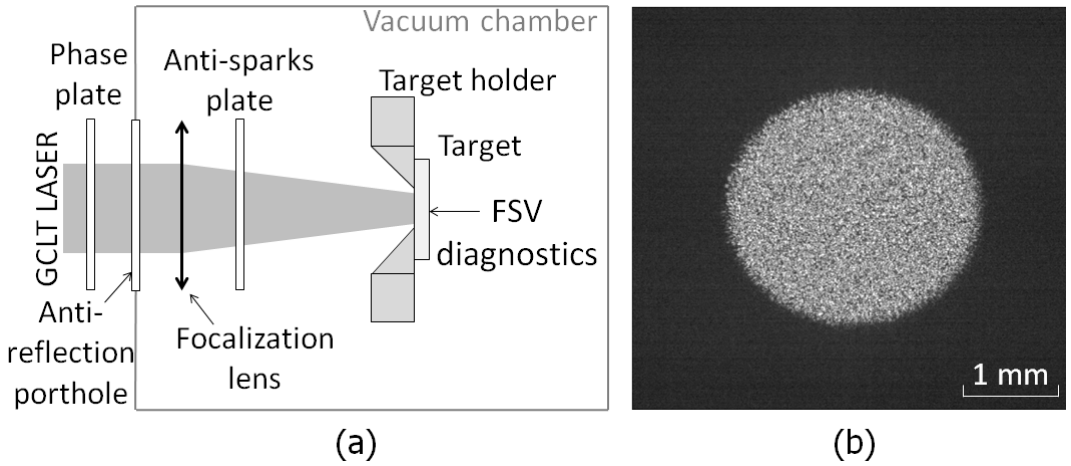

Figure 7: (a) Schematic view of the experimental set-up used on GCLT (b) Typical CCD image of a $\phi = 3,2\ mm$ focal spot

distribution. Phase-plates are placed as close as possible to the focusing lens. An anti-sparks plate, located between the target and the focusing lens as shown on Figure 7 (a), prevent any degradation from front-face particles ejection. Figure 7 (b) shows a typical spatial top-hat focal spot obtained by CCD imaging. A 532-nm VISAR system enables Free Surface Velocity (FSV) measurements of the aluminum target along time [39]. Uncertainty on the intensity $I(t)$ (ϵ_I) deposited in the axis of the VISAR spot is calculated for each laser shot by convolution of uncertainty on measured energy (E), temporal profile, spatial distribution and uncertainty on GCLT focal spot - VISAR spot alinement. A large set of experiments was realized in these conditions, within the $0,5 - 500\ GW/cm^2$ range and pulse durations from $\tau = 5\ ns$ to $40\ ns$. It enabled to provide reliable experimental data for this study.

3.1.2. Model validation

Data extracted from the experiments are used as inputs or comparative outputs for numerical model validation. The pulse temporal profile ($I(t)$) and the laser wavelength (λ) are entered in the cell stacking of ESTHER as a solicitation on the external cell. Both internal and external cells are free to move. The velocity of the internal cell is recorded as nominal numerical FSV. Different simulations are run with $I(t) - \epsilon_I$ and $I(t) + \epsilon_I$ as input data, in order to generate numerical FSV curves representative of the energy source term uncertainty. For each shot, numerical and experimental FSV curves are then plotted together and compared. The shock generated by laser-matter interaction propagates through the target thickness and generates a fast increase of the FSV, followed by a slower decrease which characterizes the release wave coming out onto the target free surface. Validation of laser-matter interaction model must then be achieved using thin targets of thickness in the 100 μm-200 μm range in order to minimize material properties influence on the FSV curves [40]. For each shot of the above-described set of experiments in the $1 - 500\ GW/cm^2$ range, a good correlation between numerical and experimental curves was observed, as shown on Figure 8. Taking ϵ_I into account, maximal values of numerical FSV curves correspond to experimental ones. In addition, shapes and durations of FSV numerical peaks are very similar to what is observed in experiments. These observations account for a good reproduction of the laser-generated ablation pressure ($P_{abl}(t)$) by the code, whatever the pulse duration and the temporal pulse shape. The laser-matter interaction model integrated to ESTHER is then validated as predictive tool with $+/-15$ % of accuracy on $P_{abl}(t)$, regarding $\epsilon_I \leq 20\%$ and the $P_{abl,max} - I_{max}$ dependency expressed in the following part. Below $1\ GW/cm^2$, FSV peaks are of much smaller amplitude ($< 20\ m/s$). FSV measurement uncertainty ϵ_v is evaluated in this work as $\approx 5\ m/s$, based on a previous study [41]. Taking into account ϵ_v and ϵ_I, there is no possibility of valuable comparison in these conditions.

3.1.3. Pressure laws

Ablation pressures profiles ($P_{abl}(t)$) can be extracted from ESTHER simulations. It is therefore possible to compare numerical results obtained with the above-described direct irradiation regime model to other models or experimental results. On Figure 9, maximal values of ablation pressures ($P_{abl,max}$) are plotted against maximal values of the temporal

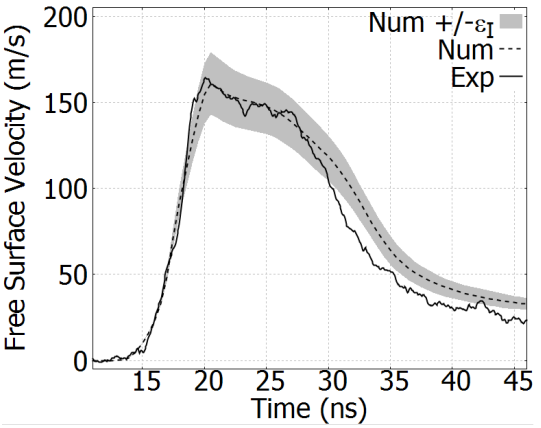

Figure 8: Experimental and numerical FSV curves of 100 μm-aluminum target under direct laser irradiation - 25 GW/cm^2 - Temporal top-hat - $\tau = 10$ ns - $\phi = 2,2$ mm

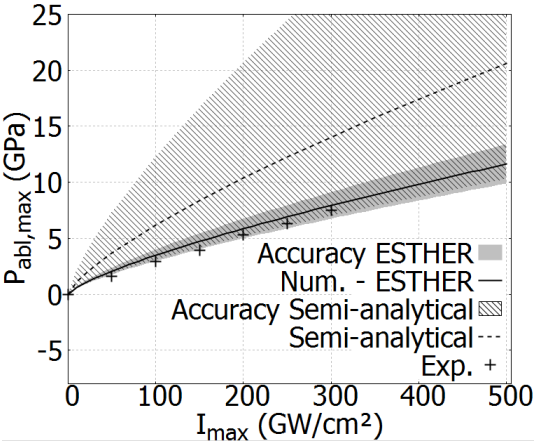

Figure 9: Evolution of $P_{abl,max}$ with I_{max} according to ESTHER, previous experiments [43] and the reference semi-analytical model [42] for $\lambda = 1064$ nm - $\tau = 25$ ns FWHM - Gaussian pulses

intensity profile (I_{max}) for $\tau = 25$ ns FWHM - Gaussian pulses at $\lambda = 1064$ nm. Results obtained with ESTHER are compared to results from a semi-analytical model [42] and experimental points determined by inverse methodology [43]. Pressure-intensity dependency is the same in the three exposed cases and can be expressed as follows: $P_{abl,max} \propto I_{max}^{0,75}$. ESTHER results are similar to experimental ones, taking into account ϵ_I. They differ significantly from the semi-analytical model's results. However, taking into account the estimated accuracy on $P_{abl,max}$ of this last model, ESTHER seems in accordance with this model. Similar studies have been led with ESTHER to identify pressure-duration and pressure-wavelength dependencies. The results of these studies enable to determine a scaling law for Gaussian pulses (Equation 13), comparable to the one of the semi-analytical model.

$$P_{abl,max}[GPa] = 1,2.10^{-3}.I_{max}[GW/cm^2]^{0,75}.\tau[s]^{-0,125}.\lambda[cm]^{0,25} \tag{13}$$

3.2. Water Confined Regime

3.2.1. Experimental facility

All water-confined experiments of this study are realized on the Hephaïstos laser facility of the PIMM laboratory (Laboratoire Procédés et Ingénierie en Mécanique et Matériaux). This table-top Nd-YAG source is composed of two independant laser beams (respectively A and B). These two laser beams follow the same optical path from the laser

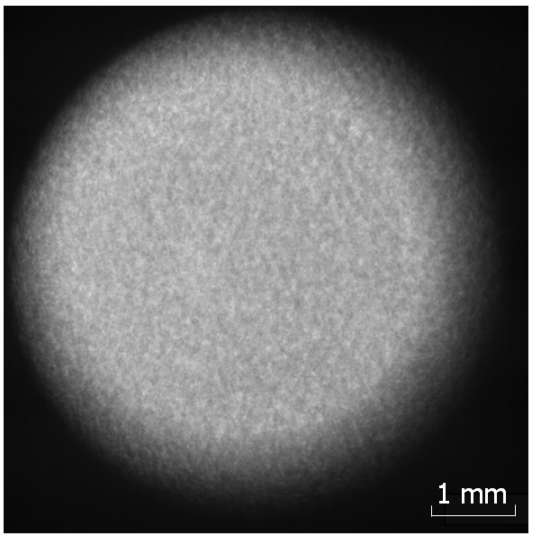

Figure 10: Typical CCD image of a $\phi = 6\ mm$ focal spot with phase-plate

source output to the target front face. This arrangement enables generation of two successive laser pulses, separated by an adjustable delay ($0\ ns < \Delta t < 1000\ ns$), allowing double-pulse configurations. Both laser beams are subjected to frequency doubling from 1064 *nm* to 532 *nm*. Each beam is able to generate $7 - ns$ FWHM Gaussian laser pulses up to 7 J. Perfect synchronization of A and B beams enable then to deposit energies up to 14 J on the target front face. Significant improvement of the on-target spatial distribution of energy has been achieved through phase plates use. Figure 10 shows an example of energy spatial distribution. It has to be noticed that local extrema within the focal spot are significantly smoothed, lowering then ϵ_I. The experimental configuration used on this facility is similar to the one presented previously, unless experiments are led in air-free conditions and a thin layer of water is applied on the target front face. FSV measurements are also achieved with a 532-nm VISAR system. Single-pulse experiments were realized in these conditions within the $0,1-7\ GW/cm^2$ range and double-pulse experiments in the $0,3-1,2\ GW/cm^2$ range, with associated delays such as $100\ ns < \Delta t < 400\ ns$.

3.2.2. Adaptation of the numerical model to WCR conditions

The numerical model previously exposed and validated in direct interaction regime is slightly modified for WCR calculations. Water cells are added on the the external side of the aluminum cell stacking. The behavior of water must be described in a large range of states, from liquid to plasma state and even in the WDM field. However, very few experimental data refer to water in the WDM regime and, contrarily to aluminium, reconstruction by interpolation of optical constants and conductivity in WDM field is complicated because of the two-atoms specificity of water. Optical constants of water cells are thus fixed at ambient conditions for $\lambda = 532\ nm$ ($n_1 = 1,33$ and $n_2 = 0$) [29]. These values enable to take into account incident laser beam reflection at air-water interface ($R = 0,04$) and no absorption is permitted through the water layer. This hypothesis ensures complete absorption of the laser beam within the aluminum target. The WCR model is therefore based on the same absorption phenomena than the one above-exposed for direct interaction regime. Thermal and hydrodynamic exchange is allowed at the water-aluminum interface. Hydrodynamic behavior of water is described by a tabulated EOS, inspired from Zamyshlyaev and Menzhulin model [44]. Electronic contribution to ionization is taken into account by a typical Zel'dovich-Raizer formulation [45]. This EOS enables to describe the evolution of water state (T, ρ, P) in each concerned cell and to take into account the acoustic confining action of the water layer on plasma. The overall water layer thickness must be higher than 500 μm to prevent perturbations of plasma behavior by water-front face release waves.

3.2.3. Model validation

The validation of the WCR model is realized using the same procedure than the one employed for direct interaction regime and exposed here-above. Taking into account ϵ_I, numerical and experimental FSV curves exhibit a good correlation in the $0,2 - 7\ GW/cm^2$ range, as exposed on Figure 11. Numerical FSV peaks show the same shape,

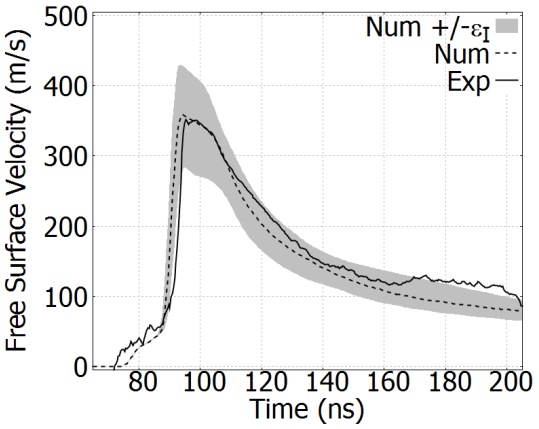

Figure 11: Experimental and numerical FSV curves of 500 μm-aluminum target under WCR irradiation - $3,0\ GW/cm^2$ - Temporal Gaussian - $\tau = 7\ ns$ FWHM- $\phi = 4,0\ mm$

durations and amplitude than the one obtained in the experiments. The adaptation of the numerical model ensures then a good reproduction of the laser-generated ablation pressure ($P_{abl}(t)$) in WCR. In this regime, ESTHER WCR model is validated with $+/-15$ % of accuracy on $P_{abl}(t)$, considering $\epsilon_I \leq 30\%$ and $P_{abl,max} - I_{max}$ dependency exposed in the following part. Below $0,2\ GW/cm^2$, higher discrepancy was found between numerical and experimental results. The thermal conduction model employed in ESTHER might be insufficient in these cases. In addition, the relevance of water conductivities in the WDM field, typical of these low intensities, must be questioned. Further works on thermal conduction data and modeling should be led if a major interest arises for laser-mater interaction in these very specific conditions.

3.2.4. Pressure law

Similarly to direct irradiation regime, numerical results obtained with ESTHER WCR model are compared on Figure 12 to experimental and analytical results. Experimental results were obtained recently in the same conditions than the ones used for this study ($\tau = 7\ ns$ FWHM - Gaussian single-pulses at $\lambda = 532\ nm$ on Hephaïstos) [38]. The comparative analytical model has been specifically designed for WCR and has been since then considered as a reference for ($P_{abl,max}$) predictions in water-confined experiments [14]. However, this analytical tool contains a physical parameter (α) that has to be calibrated using experiments. Based on experimental points exposed on Figure 12, $\alpha = 0,6$ has been identified as the optimal value [38, 46]. ESTHER results are very closed to experimental ones, taking into account ϵ_I and uncertainties on experimental points determined by inverse methodology (Figure 12). Pressure-intensity dependency is the same for both analytical and numerical models. It can be expressed as follows: $P_{abl,max} \propto I_{max}^{0,5}$. The adaptation of ESTHER to WCR conditions is good enough for pressure predictions, regarding the mentioned field of application. Scaling laws for $P_{abl,max}$ predictions can be defined using ESTHER. The Equation 14 enables to determine maximal values of $P_{abl,max}$ for $\lambda = 532\ nm$ 7 ns FWHM Gaussian pulses.

$$P_{abl,max}[GPa] = 2,4.I_{max}[GW/cm^2]^{0,5} \tag{14}$$

3.2.5. Double-Pulse configuration

The relevance of ESTHER WCR model for double-pulse configuration is evaluated by comparing FSV outputs to experimental ones that have been generated on Hephaïstos facility. All double-pulse experiments were realized using phase plates, enabling a significantly lower uncertainty on the source term ($\epsilon_I = 11\%$). Numerical FSV curves reproduce quite accurately experimental ones in the range of interest ($0,3 - 1,2\ GW/cm^2$ with $100\ ns < \Delta t < 400\ ns$), as shown on Figure 13 (a). Synchronization of second pulse-generated peak (2) is excellent. FSV increment due to the second pulse is well reproduced and discrepancy between numerical and experimental signals is not higher for the second pulse peak than for the first one (1). Peak shapes are also quite similar, despite higher amplitude modulations on the numerical curve. The numerical model developed for WCR single-pulse configurations gener-

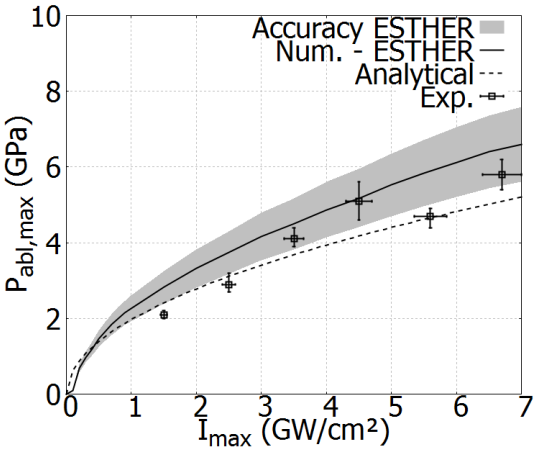

Figure 12: Evolution of $P_{abl,max}$ with I_{max} according to ESTHER, previous experiments [38] and the reference analytical model [14] for $\lambda = 532\ nm$ - $\tau = 7\ ns$ FWHM - Gaussian pulses

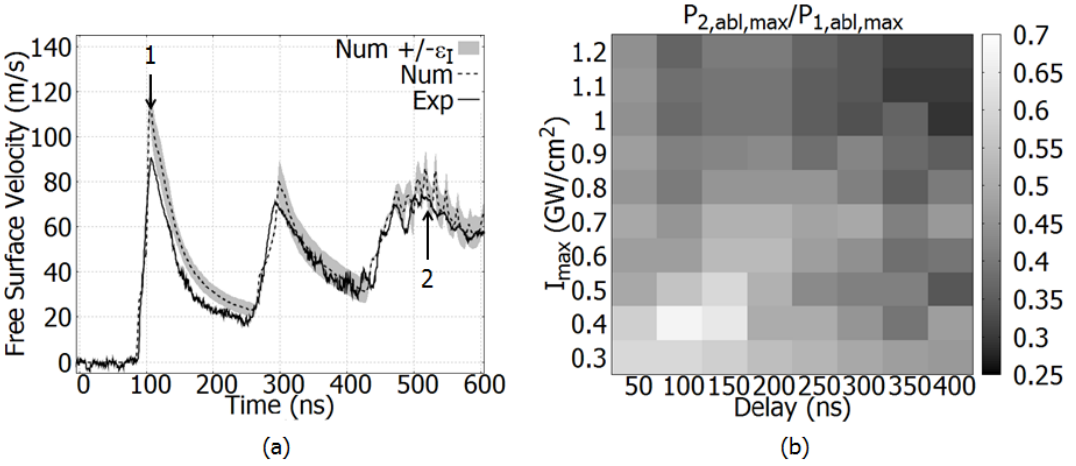

Figure 13: (a) Experimental and numerical FSV curves of 500 μm-aluminum target under WCR irradiation - $I_{1,max} = I_{2,max} = 0,7\ GW/cm^2$ - $\Delta t < 400\ ns$ - Temporal Gaussians - $\tau = 7\ ns$ FWHM - $\phi = 8,0\ mm$ - Second pulse-generated peak appears at 480 ns and b) Evolution of the $P_{2,abl,max}/P_{1,abl,max}$ ratio with I_{max} and Δt for two successive Gaussian pulses such as $I_{max} = I_{1,max} = I_{2,max}$, $\lambda = 532\ nm$, $\tau = 7\ ns$ FWHM, separated with $0\ ns < \Delta t < 400\ ns$

ates rather good results in double-pulse configuration, without additional adaptation. ESTHER WCR model is then a quite reliable tool for ablation pressures prediction in the double-pulse configurations considered in this study. Using ESTHER for P_{abl} predictions in double-pulse configuration enables the determination of laser-matter interaction efficiency ($P_{2,abl,max}/P_{1,abl,max}$) along with I_{max} and Δ_t. The results of such a study with $I_{max} = I_{1,max} = I_{2,max}$ in the $0,3 - 1,2\ GW/cm^2$ and $0\ ns < \Delta t < 400\ ns$ range are shown on Figure 13 b). All experimental FSV curves with equal intensity on both peaks ($I_{1,max} = I_{2,max}$) exhibit a lower peak associated to the second pulse than the first one. This observation has already been reported in a previous work [46]. It implies a decrease in the laser matter-interaction ($P_{2,abl,max} < P_{1,abl,max}$), whatever I_{max} and Δ_t. The diagram on Figure 13 b) corroborates this observation and shows also that the interaction intensity decreases with higher laser intensities and delays. Double-pulse configurations design for LASAT application should then be achieved by taking these limitations into account. In particular, higher intensity should be used on second pulse in order to generate double-pulse irradiation configuration with equal pressure on both pulses. It shows also that there is a very limited interest for delays higher than 400 ns for LASAT application, due to pressure decay with Δt.

Table 2
Optimal SCG parameters defined for 6061 Aluminum

Y_0 (MPa)	β	n	ϵ_i	G_0 (GPa)	G'_P	G'_T (GPa/K)	Y_{max} (MPa)
400	5500	0,10	0	27,6	1,79952	$-1,70016.10^{-2}$	500

3.3. Shock propagation in multi-materials stacks

Modeling multi-materials stacks behavior under shock loading implies to characterize each constitutive material independently, in order to choose, adapt and validate appropriate material models with a suitable set of experiments. An assembly model is then built by adding all layers successively with their corresponding material models. Validation of the assembly model is then achieved by comparing numerical FSV curves to experimental ones generated by laser pulse experiments without damaging. Another suitable set of experimental data generated at higher intensities should finally enable identification of inter-layer mechanical strengths. The application of such methodology is here exposed in the case of a 6061 Aluminum (800 μm) / Epoxy (150 μm) / 6061 Aluminum (600 μm) assembly subjected to single-pulse laser-induced shock loading. Numerical results are achieved with ESTHER and compared to the ones given by a 2D-code.

3.3.1. Materials behavior under shock loadings

As previously exposed, ESTHER is able to accurately describe hydrodynamic behavior of materials subjected to shock loadings. However, reproduction of laser-shock experiments at moderate intensities requires also to take their mechanical behavior into account [28]. In addition, LASAT application modeling imply damaging properties implementation. Shock wave experiments have then been led in various intensity regimes in order to generate a sufficient set of experimental data for highlighting hydrodynamic, mechanical and damaging behavior of 6061 Aluminum. Epoxy behavior is supposed to be largely dependent of conditions of use, whether it is shocked as bulk material or employed as thin bonding layer within a multi-materials stack. No specific model is therefore developed in this work for epoxy as mono-material. An existing model is used and adapted to reproduce epoxy behavior in the assembly model [47].

The tabulated Sesame EOS used for laser-matter interaction modeling on aluminum has already been used to model shock propagation in 6061 Aluminum [28]. In the present study, a more discriminating experimental configuration has been used to verify the relevance of such EOS for this specific alloy. In order to maximize the hydrodynamic component and minimize mechanical properties influence on FSV curves, thin 6061 Aluminum targets (50 μm-100 μm) are subjected to high-pressure laser-generated shocks ($P_{abl,max} > 10\ GPa$). Comparison of FSV curves reveals a satisfying reproduction of experimental results by the numerical model, as shown on Figure 14 (a). The first peak amplitude is accurately determined, as well as its shape and duration when ϵ_I is taken into account. The slight chemical composition discrepancy between pure and 6061 Aluminum seems to not interfere too much in the hydrodynamic behavior. The tabulated EOS used here is therefore able to describe both laser-matter interaction and hydrodynamic component of shocks in 6061 Aluminum. In this study, the same EOS is then used in the whole cell stack, preventing any perturbations due to EOS change through the target thickness.

The mechanical behavior of 6061 Aluminum under laser-generated shock waves has already been characterized in a previous study [48]. The same Steinberg-Cochran-Guinan (SCG) model has been choosen here [49]. Specific experiments have been realized on thicker targets (250 μm-500 μm) at lower pressures ($0\ GPa > P_{abl,max} > 3\ GPa$), in order to highlight the elastic precursor and the elasto-plastic shock response. Modeling these experiments enables to evaluate the relevance of this model in the case of 6061 Aluminum subjected to moderate shocks. Small modifications of SCG parameters were necessary to describe more accurately the mechanical behavior of 6061 Aluminum, as exposed on Figure 14 b). For all experiments realized in similar conditions, elastic precursor amplitude is very well reproduced, implying a good identification of the material yield strength. In addition, the second peak synchronization is very good, which highlights a good reproduction of the whole elasto-plastic field. The final set of S-C-G parameters, given in Table 2, is then validated for 6061 Aluminum mechanical behavior modeling.

The damaging behavior of 6061 Aluminum was previously characterized in very near conditions than the ones considered in this study [48]. We used here the same Johnson model to fit spall experiments realized on both Hephaïstos and GCLT facilities [50]. High-pressure shocks ($P_{abl,max} > 10\ GPa$) have been employed in order to initiate damaging and generate spallation. Two minor modifications were brought on the previously defined set of parameters in order to increase the accuracy of the numerical model. α_0 was slightly increased from 1,0003 to 1,0004 and a_s lowered from 180 MPa to 130 MPa. α_0 modification enables to reduce the evolution range of porosity. Decreasing of a_s induces

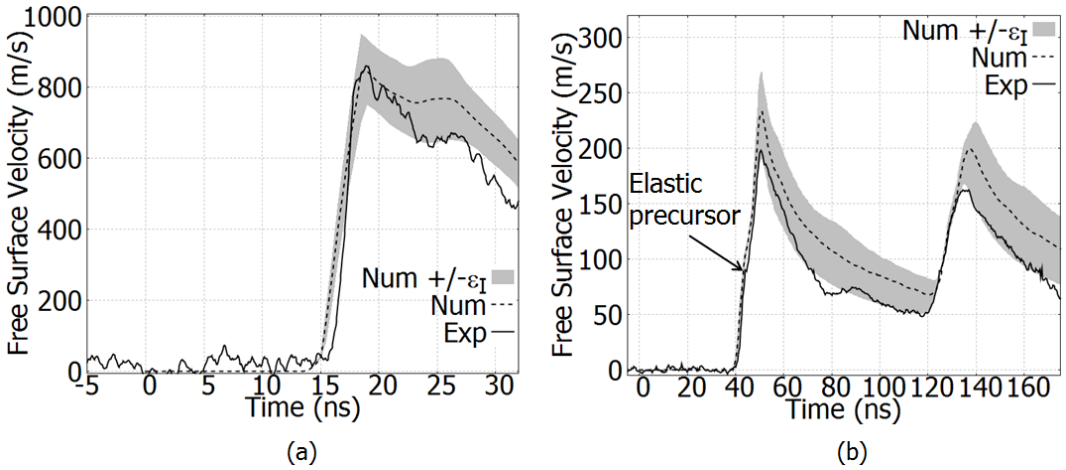

Figure 14: Experimental and numerical FSV curves of 6061 Aluminum targets under laser irradiation (a) 100 μm- thick target exposed to GCLT - 300 GW/cm^2 - Temporal top-hat - $\tau = 10$ ns - $\phi = 1$ mm - $\epsilon_I = 11\%$ in direct irradiation regime (b) 250 μm- thick target exposed to Hephaïstos - $1,1$ GW/cm^2 - Gaussian - $\tau = 7$ ns FWHM - $\phi = 4$ mm - $\epsilon_I = 30\%$ in WCR

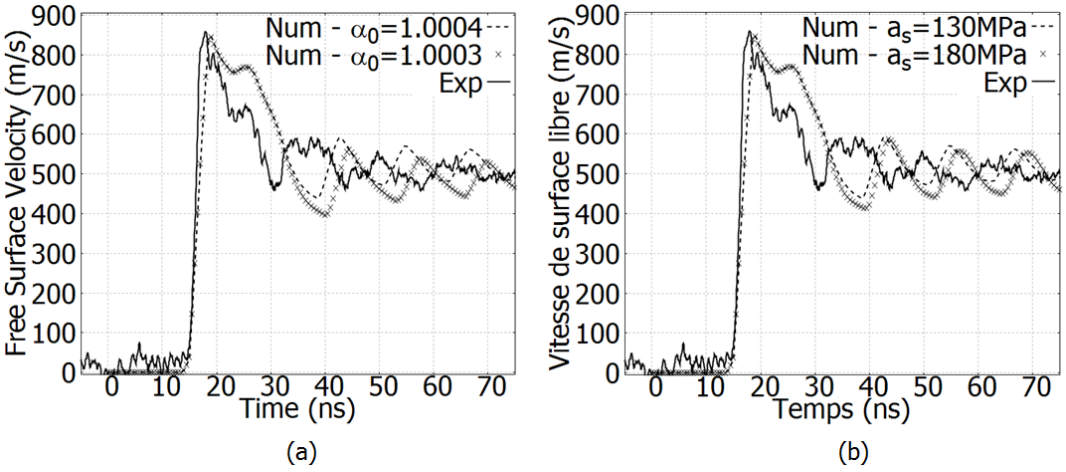

Figure 15: Experimental and numerical FSV curves of 6061 Aluminum targets under laser irradiation - 100 μm- thick target exposed to GCLT - 300 GW/cm^2 - Temporal top-hat - $\tau = 10$ ns - $\phi = 1$ mm - $\epsilon_I = 11\%$ in direct irradiation regime (a) Modification of α_0 (b) Modification of a_s

Table 3
Optimal Johnson parameters defined for 6061 Aluminum

a_s (MPa)	α_0	eta (Pa/s)	α_{lim}
130	$1,0004$	$0,54$	$1,05$

a lower stress to initiate damaging. The new set of parameters facilitates material failure, hence quicker spallation and higher ballistic velocity, as shown on Figure 15 (a) and (b). On this Figure, laser-matter interaction model generates a quite longer pressure profile than the experimental one. However, the new set of parameters enhances the correlation with the experimental FSV curve. Both changes are then required. The newly defined set of parameters is exposed on Table 3.

Table 4
Mechanical tensile strengths of two different bonding qualities on 6061 Aluminum (800 μm) / Epoxy (150 μm) / 6061 Aluminum (600 μm) assembly

	$\sigma_{threshold,LASAT}$ (MPa)	$\sigma_{threshold,static}$ (MPa)
Quality 1	175	15,8 +/- 3,3
Quality 2	350	36 +/- 3,6

3.3.2. Assembly model validation

A set of single-pulse experiments has been led on GCLT facility on the assembly of interest for this study (6061 Aluminum (800 μm) / Epoxy (150 μm) / 6061 Aluminum (600 μm)). Laser illumination ($\phi = 3,2\ mm$) is applied on the thicker substrate and VISAR diagnostics is employed on the free surface. For a given pulse shape, pulse duration and focal spot diameter, variation of energy is applied to generate a large range of pulse intensities. Non-destructive testing (NDT) and post-shock micrographs of the post-shock sample enables to detect defects within the assembly. A disbond threshold has been identified using this technique but no damage has been found in 6061 Aluminum substrates. The experimental FSV curve exposed on Figure 16 (b) is taken out from the set of undamaged assemblies results and it is considered as the reference for numerical-experimental comparison. A first observation is that the signal is hardly understandable, contrarily to mono-material FSV curves. The assembly model is built using the 6061 Aluminum material model, coupled to the laser-matter interaction introduced in this document. Between both 6061 Aluminum substrates, a layer of epoxy is introduced. The epoxy behavior under shock loading is realized using a Puff-Mie-Grüneisen (PMG) EOS, coupled to an Elastic-Perfectly-Plastic (EPP) mechanical model, identified in a previous study [47]. Using this assembly model enables to reproduce the experimental results with an overall good agreement. The origin of each shock breaking out on the free surface can thus be determined using a time-position diagram generated with ESTHER outputs, such as the one employed on Figure 16 (a). This tool shows that most of FSV increments are due to impedance mismatches between the epoxy layer and both substrates. An other numerical FSV curve has been generated with a 2D-axis-symmetrical simulation led with the same material models and the ablation pressure profile generated with ESTHER, introduced as source term. Despite some small discrepancies induced by focal spot edges-effects (i.e. for $350\ ns < t < 400\ ns$), numerical FSV curves are very similar. Larger difference is observed for $t > 1000\ ns$, when 2D effects become dominants. ESTHER code with the associated numerical models is then validated for shock propagation modeling in the assembly presented here.

3.3.3. Identification of bond mechanical strength

Determination of the epoxy layer mechanical strength is determined using a FSV signal of a disbonded assembly. Numerical calculation of this experiment is realized using the validated assembly model. A cut-off model is then added to the epoxy material model and calculations are run with different cut-off strength values ($\sigma_{threshold}$). Comparison of numerical outputs with the reference experimental is then realized and the best numerical-experimental correlation is determined. The corresponding numerical signal defines the epoxy layer bond mechanical strength. In the case exposed on Figure 17 (b), FSV oscillations of the experimental curve for $t > 880\ ns$ are well reproduced by the numerical model with $\sigma_{threshold} = 165\ MPa$, whereas a significant discrepancy is visible between the numerical signal without damaging model and the experimental one. The stress history at both substrate/epoxy interfaces generated with ESTHER and exposed on Figure 17 (a) enables to determine the disbonding time ($t = 730\ ns$) and localization (interface 1). Disbonding generates free surfaces at the first interface, which modify the shock propagation pattern and thus the FSV curve exposed on Figure 17 (b). The same procedure has been applied on a higher bond quality and $\sigma_{threshold} = 350\ MPa$ was found. The methodology here exposed has then allowed to discriminate two different bonding qualities on the considered assembly by determination of respective mechanical strengths. Table 4 exposes results obtained on both assembly qualities at high (laser-induced shock) and very low (pull-out quasi-static test) strain rates. These results show an obvious correlation between high and very low strain rates mechanical strength. One order of magnitude separates results obtained with both techniques, whatever the bond quality.

4. CONCLUSION

ESTHER code has proven to be a reliable code for ablation pressure predictions in both WCR and direct irradiation regime. Validation of the corresponding laser-matter interaction numerical models has been achieved respectively in the $0,2 - 7\ GW/cm^2$ and $1 - 500\ GW/cm^2$ intensity ranges, considering appropriate experimental uncertainty

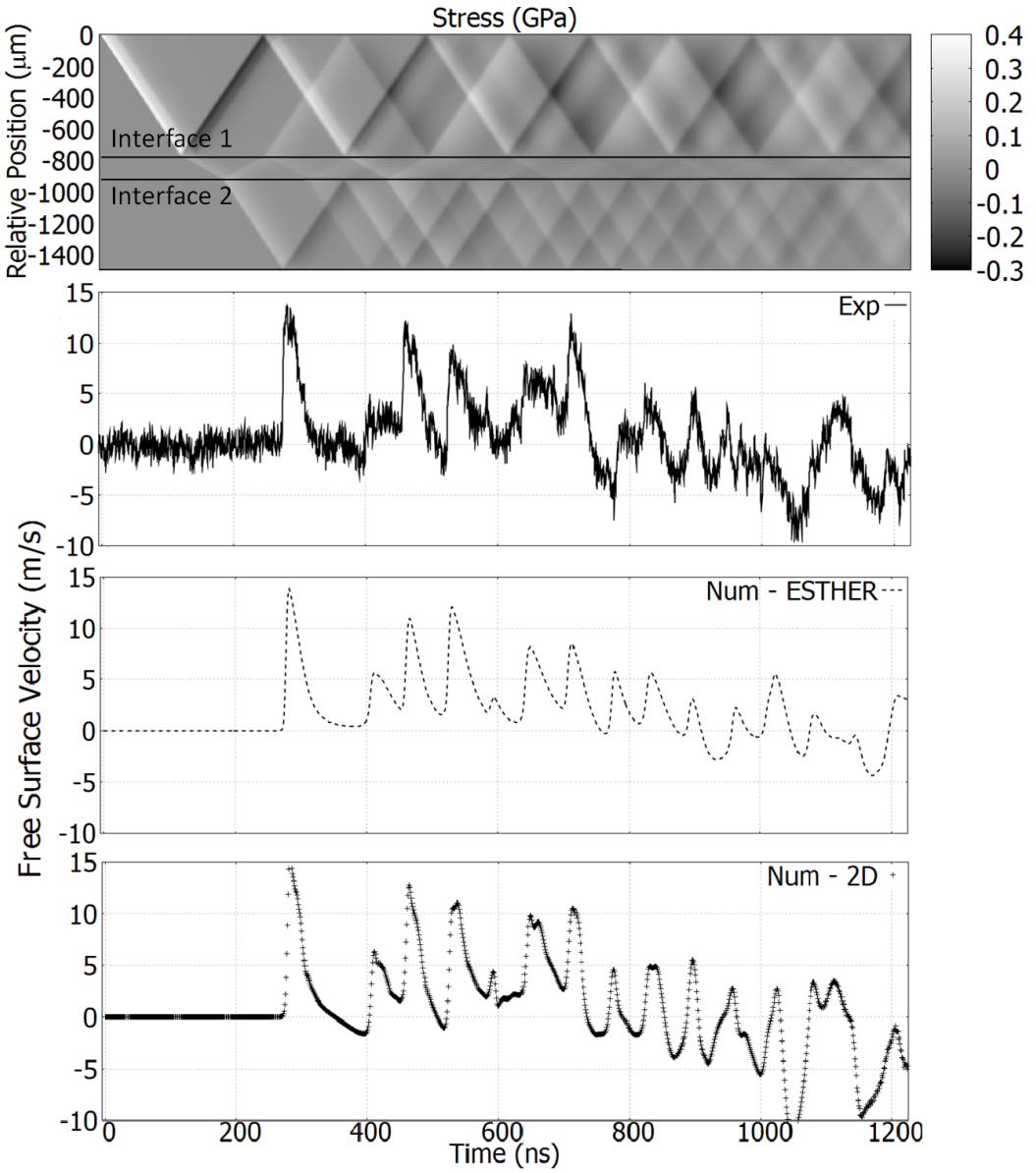

Figure 16: Experimental and numerical results of 6061 Aluminum (800 μm) / Epoxy (150 μm) / 6061 Aluminum (600 μm) under direct laser irradiation - GCLT - $2,9\ GW/cm^2$ - Temporal top-hat - $\tau = 20\ ns$ - $\phi = 3,2\ mm$ - Deduction of 20% on I corresponding to ϵ_I - (a) Time-position numerical diagram generated with ESTHER (x=0 corresponds to front face position at t=0) (b) Experimental and numerical FSV curves with ESTHER (1D) and with a 2D code

on source terms. WCR model has proven to be also quite relevant for double-pulse configurations in WCR. Further investigations should however be led on this last model in order to fit more closely to experimental curves. Specific experimental data of interest are listed in this document. The last part of this study has also shown that shock propagation in multi-material stacks can also be reproduced by ESTHER code, as long as the 1D shock propagation component is predominant. This simulation tool enhances FSV signals understanding when impedance mismatches occur. It enables also to determine inter-layer mechanical strength of a given assembly by application of the methodology exposed here.

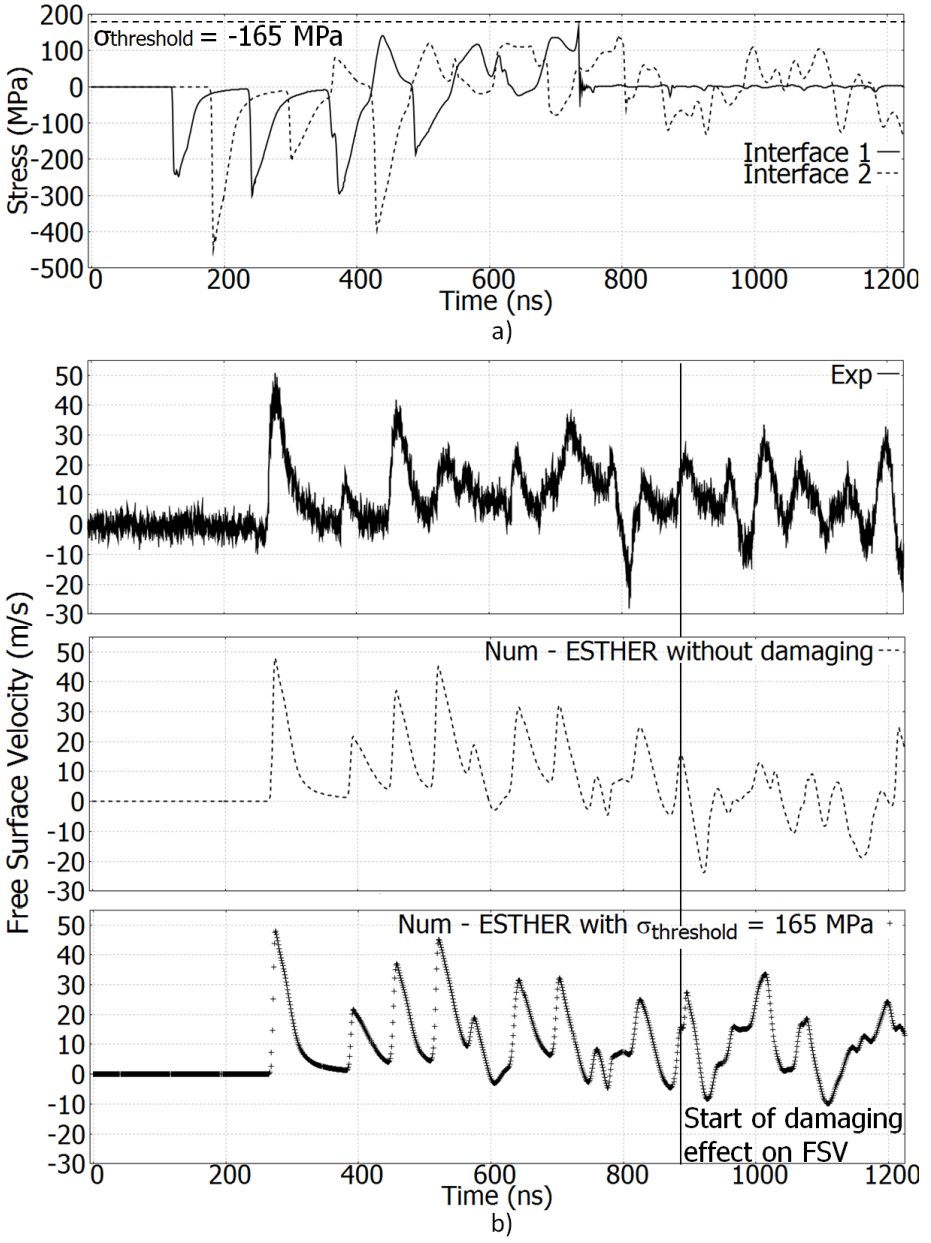

Figure 17: Experimental and numerical results of 6061 Aluminum (800 μm) / Epoxy (150 μm) / 6061 Aluminum (600 μm) under direct laser irradiation - GCLT - 16,6 GW/cm^2 - Temporal top-hat - $\tau = 20$ ns - $\phi = 3,2$ mm - Deduction of 20% on I corresponding to ϵ_I - (a) Numerical stresses in the shock propagation direction at both substrate/epoxy interfaces, generated with ESTHER (b) Experimental and numerical FSV curves with ESTHER (1D) with $\sigma_{threshold} = 165$ MPa

5. ACKNOWLEDGMENTS

We gratefully acknowledge the support of BPI France, Ile de France, Nouvelle Aquitaine regions, and competitiveness clusters ASTECH, Route des Laser and Aerospace Valley through the CompoChoc project for this work. We also wish to thank L. Dinand for samples realization.

References

[1] L. Chapman, Journal of Transport Geography **15**, 354–367 (2007).
[2] P. Lawrence, Technology analysis and strategic management **21(1)**, 79–92 (2009).
[3] J. Lee, Energy Conversion and Management **51**, 189–196 (2010).
[4] S. Cregger, "Breaking the development cost curve by using analysis," in *JEC Europe* (2015).
[5] P. Mangalgiri, Bulletin of Materials Science **22(3)**, 657–664 (1999).
[6] D. Markatos, K. Tserpes, E. Rau, S. Markus, B. Ehrhart, and S. Pantelakis, Composites: Part B **45**, 556–564 (2013).
[7] L. Berthe, M. Arrigoni, M. Boustie, J. Cuq-Lelandais, C. Broussillou, G. Fabre, M. Jeandin, V. Guipont, and M. Nivard, Nondestructive Testing and Evaluation **26**, 303–317 (2011).
[8] P. Mora, Physics of Fluids **25**, p. 1051 (1982).
[9] R. Ambartsumyan, N. Basov, V. Boiko, V. Zuev, O. Krokhin, P. Kryukhov, Y. Senat-Skii, and Y. Stoilov, Soviet Physics JETP **21 (6)**, 1061–1064 (1965).
[10] A. Caruso, B. Bertotti, and P. Giupponi, Il Nuovo Cimento **45**, 176–189 (1966).
[11] L. Veeser, Physical Review Letters **40**, 1391–1394 (1966).
[12] J. Fox, Applied Physics Letters **24**, 461–464 (1974).
[13] N. Anderholm, Applied Physics Letters **16**, 113–115 (1970).
[14] R. Fabbro, J. Fournier, P. Ballard, D. Devaux, and J. Virmont, American Institute of Physics **68**, p. 775 (1990).
[15] L. Berthe, R. Fabbro, P. Peyre, L. Tollier, and E. Bartnicki, Journal of Applied Physics **82 (6)**, 2826–2832 (1997).
[16] L. Berthe, "Processus de claquage des milieux transparents sous irradiation laser. application au choc laser en regime de confinement par eau," Ph.D. thesis, Universite Paris XI 1998.
[17] A. Sollier, "Etude des plasmas generes par interaction laser-matiere en regime confine. application au traitement des materiaux par choc laser," Ph.D. thesis, Universite de Versailles - Saint Quentin en Yvelines 2002.
[18] T. Antoun, L. Seaman, and D. Curran, *Spall fracture* (Springer Verlag, 1997).
[19] E. Gay, L. Berthe, E. Buzaud, M. Boustie, and M. Arrigoni, Journal of Applied Physics **114**, p. 502 (2012).
[20] R. Ecault, "Etude experimentale et numerique du comportement dynamique de composites aeronautiques," Ph.D. thesis, Ecole Nationale Superieure de Mecanique et d'Aerotechnique 2013.
[21] B. Wu and Y. Shin, Journal of Applied Physics **97**, p. 113517 (2005).
[22] B. Wu and Y. Shin, Applied Physics Letters **88**, p. 041116 (2006).
[23] B. Wu and Y. Shin, Journal of Applied Physics **101**, p. 023510 (2007).
[24] J. Colombier, P. Combis, F. Bonneau, R. Le Harzic, and E. Audouard, Physical Review B **71**, p. 165406 (2005).
[25] J. Cuq-Lelandais, M. Boustie, L. Berthe, T. de Resseguier, P. Combis, J. Colombier, M. Nivard, and A. Claverie, Journal of Physics D: Applied Physics **42**, p. 065402 (2009).
[26] P. Leguay, A. Levy, B. Chimier, F. Deneuville, D. Descamps, C. Fourment, C. Goyon, S. Hulin, S. Petit, O. Peyrusse, J. Santos, P. Combis, B. Holst, V. Recoules, P. Renaudin, L. Videau, and F. Dorchies, Physical Review Letters **111**, p. 245004 (2013).
[27] S. Laffite, S. Baton, P. Combis, J. Clerouin, M. Koenig, V. Recoules, C. Rousseaux, and L. Videau, Physics of Plasmas **21**, p. 082705 (2014).
[28] S. Bardy, B. Aubert, L. Berthe, P. Combis, D. Hébert, E. Lescoute, J. L. Rullier, and L. Videau, Optical Engineering **56 (1)**, p. 011014 (2016).
[29] E. Palik, *Handbook of Optical Constants* (Academic Press, London, 1998).
[30] L. Spitzer, *Physics of fully ionized gas* (Dover Publications, New-York, 1962).
[31] M. Born and E. Wolf, *Principles of Optics* (Pergamon Press Ltd, London, 1959).
[32] Y. Touloukian, *Thermophysical properties of matter* (IFI/Plenum, New-York, 1970).
[33] G. Faussurier, C. Blancard, P. Cossé, and P. Renaudin, Physics of Plasmas **17**, p. 052707 (2010).
[34] C. Blancard and G. Faussurier, Physical Review E **69**, p. 016409 (2004).
[35] M. Modest, *Radiative heat transfer* (Academic Press, 2013).
[36] A. Decoster, Rapport des activités laser, Comissariat à l'Energie Atomique, Limeil-Valenton (1994).
[37] D. Bergstrom and A. Kaplan, Journal of Applied Physics **103**, p. 103515 (2008).
[38] D. Courapied, "Interaction laser-matière en régime de confinement par eau avec deux impulsions laser - application au test d'adhérence par choc laser," Ph.D. thesis, Ecole Nationale Supérieure d'Arts et Métiers 2016.
[39] L. M. Barker and R. Hollenbach, Journal of Applied Physics **43(11)**, p. 4669 (1972).
[40] S. Bardy, "Contrôle et optimisation du test d'adhérence par choc laser sur assemblages collés," Ph.D. thesis, Ecole Nationale Supérieure d'Arts et Métiers 2017.
[41] D. Dolan, Sandia National Laboratories report (4 April 2006).
[42] C. R. Phipps, T. Turner, R. Harrison, G. York, W. Osborne, G. Anderson, X. Corlis, L. Haynes, H. Steels, and T. Spicochi, Journal of Applied Physics **64**, p. 1083 (1988).
[43] L. Tollier, "Caractérisation de chocs-laser a éclairements modérés par interférometrie doppler visar. application a l étude de l'endommagement par écaillage de matériaux métalliques." Ph.D. thesis, Université de Poitiers 1996.
[44] B. V. Zamyshlyaev and M. Menzhulin, Journal of applied mechanics and technical physics **12(3)**, 445–450 (1971).
[45] Y. B. Zel'dovich and Y. P. Raizer, *Physics of Shock Waves and High-Temperature Hydrodynamic Phenomena* (Dover Publications, Inc., New-York, 1967).
[46] L. Berthe, D. Courapied, S. El Karnighi, P. Peyre, C. Gorny, and Y. Rouchausse, Journal of Laser Applications **29(4)**, p. 042006 (2017).
[47] D. Laporte, "Analyse de la réponse d'assemblages collés sous des sollicitations en dynamique rapide," Ph.D. thesis, Ecole Nationale Supérieure de Mécanique et d'Aérotechnique 2011.
[48] B. Jodar, Master's Thesis - Technische Universität Braunschweig (12 December 2014).
[49] D. Steinberg, S. Cochran, and M. Guinan, Journal of Applied Physics **51**, p. 1498 (1980).

[50] J. Johnson, Journal of Applied Physics **52**, p. 2812 (1981).